Appl. Sci. **2014**, *4*, 180-194; doi:10.3390/app4020180

OPEN ACCESS

applied sciences

ISSN 2076-3417

www.mdpi.com/journal/applsci

Article

Mechanism of Thin Layers Graphite Formation by ^{13}C Implantation and Annealing

Gaelle Gutierrez, François Le Normand *, Fitsum Aweke, Dominique Muller, Claude Speisser and Frédéric Antoni

ICube-Laboratoire des Sciences de l'Ingénieur, de l'Informatique et de l'Imagerie, Université de Strasbourg-CNRS, 23, rue du Loess, Strasbourg Cedex 67037, France; E-Mails: gaellegutierrez@yahoo.fr (G.G.); fitsum.aweke@etu.unistra.fr (F.A.); d.muller@unistra.fr (D.M.); claude.speisser@unistra.fr (C.S.); frederic.antoni@unistra.fr (F.A.)

* Author to whom correspondence should be addressed; E-Mail: francois.le-normand@unistra.fr; Tel.: +33-3-88-10-6546; Fax: +33-3-88-10-6548.

Received: 31 December 2013; in revised form: 5 March 2014 / Accepted: 18 March 2014 / Published: 21 April 2014

Abstract: The mechanism of thin layers graphite (TLG) synthesis on a polycrystalline nickel film deposited on SiO_2 (300 nm thick)/Si(100) has been investigated by ^{13}C implantation of four equivalent graphene monolayers and annealing at moderate temperatures (450–600 °C). During this process, the implanted ^{13}C segregates to the surface. Nuclear Reaction Analyses (NRA) are used for the first time in the topic of graphene synthesis to separate the isotopes and to determine the ^{12}C and ^{13}C concentrations at each step. Indeed, a significant part of carbon in the TLG also comes from residual ^{12}C carbon absorbed into the metallic matrix. Raman spectroscopy and imaging are used to determine the main location of each carbon isotope in the TLG. The Raman mappings especially emphasize the role of ^{12}C previously present at the surface that first diffuses along grain boundaries. They play the role of nucleation precursors. Around them the implanted ^{13}C or a mixture of bulk ^{12}C–^{13}C aggregate and further precipitate into graphene-like fragments. Graphenization is effective at around 600 °C. These results point out the importance of controlling carbon incorporation, as well as the importance of preparing a uniform nickel surface, in order to avoid heterogeneous nucleation.

Keywords: carbon; graphene; thin layers graphite; nickel; nuclear reaction analysis; Raman spectroscopy; Raman imaging; nucleation; ^{13}C isotope

1. Introduction

Graphene is a hexagonal network of sp^2-hybridized carbon atoms, showing outstanding electronic and heat transport properties [1]. However, these transport properties will be strongly dependent on the preparation methods and a susbsequent transfer of the films. The elaboration methods involve processes, such as chemical synthesis [2], high temperature Si layer evaporation from a SiC monocrystalline surface [3,4], surface precipitation of carbon precursors absorbed into metals, such as Ni by Chemical Vapor Deposition (CVD) [5–11], surface carbon adsorption on copper by CVD [12], bulk diffusion of carbon through metallic matrices [13,14], and carbon ion implantation into a metallic matrix followed by surface segregation [15–20]. However, the transport properties will be strongly dependent on the preparation methods, and a subsequent transfer of the films as the preparation methods, described in the literature, is generally not obtained on the substrates appropriate for such applications thus far. The graphene formation through carbon implantation presents some strong potentials for application in electronic devices, such as (i) depending on the depth implantation, the possibility to diffuse carbon, either at the metallic surface, or at the interface, giving an elegant way to form graphene on a larger choice of substrates, and especially on substrates compatible with electronic devices [11]; (ii) a uniform and precise control of the implanted dose of carbon without necessity for gaseous decomposition of the carbon precursors; (iii) the possibility to dope the graphene with either N or B; and (iv) the use of isotope labeling for mechanistic studies. Nevertheless, previous results suggest that the amount of carbon observed after implantation is higher than the amount of carbon implanted. This has been explained by the incorporation of spurious carbon at each step of the process, leading to undesired heterogeneous nucleation and the formation of a large density of small fragments of thin layer graphite (TLG) [20,21]. In order to understand the mechanism of graphene formation, including the surface carbon segregation step and the graphenization step, and further to control the growth of large and thin graphene films, it is, therefore, necessary to determine, first, the role of the carbon already present, either at the surface, or in the bulk of the metallic matrix.

In this study, we use the implantation of ^{13}C labeled carbon to study the mechanisms of graphene and TLG formation. Therefore, we are able to determine the proportion, due to implanted carbon, from the proportion due to carbon coming from others contamination sources (^{13}C ions are present only in 1.1% of natural carbon). Analyses of the carbon isotopes in the TLG films were performed by Raman imaging and by Nuclear Reaction Analysis (NRA). Moreover, to activate the carbon diffusion, as well as to minimize the implantation steps in the overall synthesis process, the carbon implantations were carried out at high temperatures (450–600 °C), instead of implantation at room temperature as generally reported in the literature [15–19].

2. Experimental Section

The preparation of Ni(200 nm)/SiO_2(300 nm)/Si[100] (further named Ni/Si sample) used as a substrate for carbon implantation has already been reported elsewhere [11,20] and is summarized in Figure 1.

Figure 1. Scheme of the preparation of Ni/Si sample.

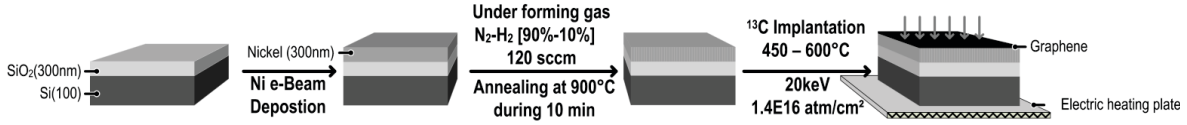

In order to induce a grain growth, and to limit the sample degassing during high temperature implantation, an initial annealing at 900 °C during 10 min, under forming gas (H_2/N_2 at 10%/90%), was performed using Rapid Thermal Annealing (RTA). The heating and cooling rates were estimated to be around 5 °C/s and 10 °C/s, respectively. The Ni/Si samples were then implanted with 20 keV ^{13}C ions at a fluence of 1.4×10^{16} at/cm^2 from a ^{13}CO source (EURISO-TOP, Saint-Aubin, France, purity 99%), corresponding to around four equivalent graphene monolayers (EGM; 1 EGM is quoted to 3.6×10^{15} at/cm^2). The implantation was carried out at 600 °C by using a heated substrate holder in Inconel alloy in a vacuum pressure of 2×10^{-6} mbar during 60 min. More details on the implantation process are given in [20]. The heating and cooling rates were around 20 °C/min for the implantation occurring at 600 °C. The temperature at the sample surface was calibrated by using both a thermocouple settled on the back of the substrate holder and an extinction pyrometer in front of the sample. The thickness of the evaporated Ni films (300 nm) was determined by Rutherford Backscattering Spectroscopy (RBS) (Figure 2). No special alteration of the steep RBS profiles can be observed on the surface side (around 1580 keV), as well at the substrate/nickel side (around 1300 keV), of the nickel film after carbon implantation at 600 °C. The relative precision of the amount of Ni, before and after implantation, by RBS measurement, is less than 2×10^{16} Ni/cm^2, corresponding to a thickness of 2 nm. Therefore, within this limit, there is no evolution of Ni layer during ion implantation by sputtering.

Figure 2. RBS profiles of the Ni/Si sample after RTA at 900 °C and ion implantation at 600 °C.

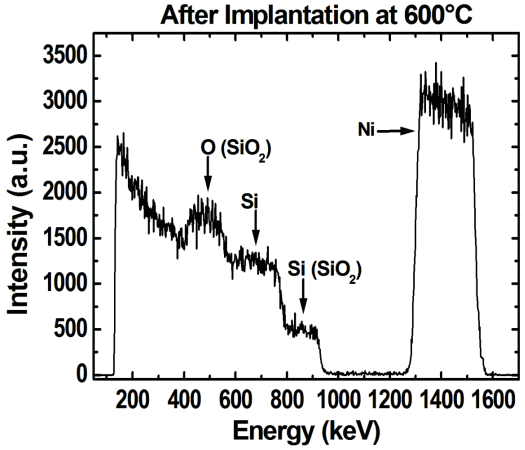

To determine the concentrations of ^{13}C and ^{12}C atoms into nickel, NRA induced by a 900 keV deuterons (^{2}H) beam through the $^{12}C(d, p)^{13}C$, $^{13}C(d, p)^{14}C$, $^{16}O(d, p_1)^{17}O$ and $^{16}O(d, p_0)^{17}O$ reactions were carried out. The measurements were performed with the 4 MeV Van de Graff accelerator of ICube laboratory. Experimental conditions for NRA were described elsewhere [20]. The spectra were calibrated by using bare SiO_2 and SiC samples for oxygen and carbon nuclear reactions, respectively, and were further analyzed with the home-made SAM software (Systeme d'Analyse des Materiaux) [22].

Samples were imaged by a Scanning Electron Microscope (SEM), a Phillips XL-30S operating at 3 kV.

The Atomic Force Microscopy (AFM) measurements were performed on a NT-MDT Stand Alone "SMENA" set-up, used in the resonant mode AFM Semicontact with non-contact "Golden" Silicon Cantilever NSG11 scanning probes.

Raman spectra on the TLG were recorded on a Horiba Jobin Yvon (Longjumeau, France) LabRam equipment with an excitation length at 532 nm and a laser fluence of 2.25 mW/μm^2, chosen to avoid damage to the graphene film during the analyses [23]. The area intensity of each Raman mode is taken for the mappings.

3. Results

3.1. NRA Measurements

Figure 3 displays the NRA spectra obtained for a Ni/Si sample at two steps of the process, before and after the ^{13}C implantation at 600 °C, respectively.

Figure 3. (**a**) NRA spectra obtained for Ni/Si samples at two steps of the process: before (black) and after (red) the ^{13}C implantation at 600 °C. In (**b**), the signal $^{13}C(d, p)^{14}C$ around 5825 keV is magnified.

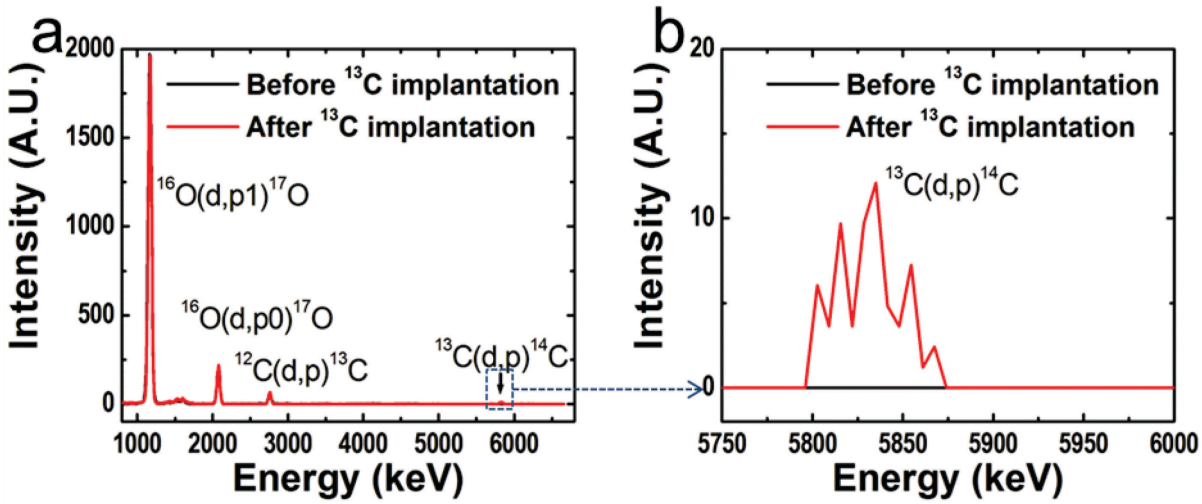

The signals appearing at around 2770 keV and 5850 keV correspond to the $^{12}C(d, p)^{13}C$ and $^{13}C(d, p)^{14}C$ nuclear reactions, with corresponding cross-sections 25.9 mb/sr [24] and 2.36 mb/sr [25], respectively. Owing to the low sensitivity of the $^{13}C(d, p)^{14}C$ reaction, the detection limit for ^{13}C signal

is quoted to no more than 1 EGM. In Table 1 the ^{12}C and ^{13}C concentrations obtained by NRA are reported at different steps of the process. The presence of a $^{12}C(d, p)^{13}C$ contribution before implantation reveals some carbon contamination.

Table 1. ^{12}C and ^{13}C concentrations obtained from $^{12}C(d, p)^{13}C$ and $^{13}C(d, p)^{14}C$ Nuclear Reaction Analysis (NRA), respectively, fitted with SAM software.

Sample (Step)	^{12}C concentration (10^{15} at·cm^{-2})	^{13}C concentration (10^{15} at·cm^{-2})
Ni/Si	21 ± 3	-
Ni/Si (after RTA at 900 °C)	17 ± 3	-
Ni/Si (after RTA 900 °C and subsequent ^{13}C implantation at 1.4×10^{16} at·cm^{-2} at 600 °C)	20 ± 3	13 ± 4
1 Equivalent Graphene Monolayer (EGM)	3.6	

Due to the low depth resolution, we were not able to differentiate the carbon contributions coming either from the surface nor diluted into the Ni layer. Thus, only the total carbon concentrations obtained by fitting the experimental spectra are reported. This contamination is measured to $(21 \pm 3) \times 10^{15}$ at·cm^{-2} corresponding to around 6 EGM. This carbon pollution very probably occurs during the Ni deposition, corresponding to a relative atomic concentration of:

$$[C]/[Ni] = [C] \times t \times S \times d_{Ni} \times N_A/M_{Ni} = 2.1 \times 10^{16}/1.6 \times 10^{18} = 1.3\% \quad (1)$$

where t is the thickness of the Ni layer (200 nm); d_{Ni} and M_{Ni} are the number density and the atomic mass of Ni (7.81 g·cm^{-3} and 58.7 g·mol^{-1}, respectively); N_A is the Avogadro number and S is the sample surface (1 cm^2). It is believed that it is an upper limit to the carbon concentration, as it is assumed in Equation (1) that the carbon is located inside the nickel film, although a significant amount of carbon is also present on the surface, as reported in [20,21]. This measured concentration is, therefore, in line with the thermodynamic phase diagram carbon-nickel [26]. Moreover, the nickel could also be contaminated during different analyses (such as SEM, *etc.*) carried out on the sample. More experiments are presently under investigations in order to find out at which steps this unexpected pollution occurs and to remove it. A small decrease of the ^{12}C concentration, down to $(17 \pm 3) \times 10^{15}$ at·cm^{-2}, can be observed after the RTA step at 900 °C. Thus, it is presumed that some carbon has been consumed by the effective hydrogenation with forming gas. After further implantation at 600 °C, the ^{13}C concentration roughly corresponds to the expected carbon dose $(13 \pm 3) \times 10^{15}$ at·cm^{-2} whereas no significant evolution of the ^{12}C concentration can be observed. Therefore, the sample after implantation contains $(33 \pm 7) \times 10^{15}$ at·cm^{-2} of overall carbon after implantation, corresponding to around 60% and 40% of the ^{12}C and ^{13}C isotopes, respectively. In conclusion, we have shown by NRA some pollution of the sample by ^{12}C carbon, mainly at the Ni deposition step, and further investigations are needed to limit, if not suppress, these sources of pollution.

3.2. Morphological Investigations (SEM, AFM)

After the RTA at 900 °C, grain boundaries of nickel clearly appear (Figure 4a). After further implantation at 600 °C, observations by SEM, in Figure 4b,c highlight the occurrence of highly contrasted dark fragments, unlike the Ni/Si bare sample, which could be assigned to TLG.

Moreover, contrast variations can be detected within these TLG (Figure 4c). They cannot be attributed to topological contrasts, as the SEM contrast used in the secondary electron mode is mainly related to the thickness of the graphene layers [20]. Some of them have facetted edges with well-defined angles. Another interesting observation is that all the TLG pieces are related to the presence of grain boundaries, mostly with the side of a TLG that superimposes a grain boundary (white arrows in Figure 4b,c) or with a TLG that crosses over one or more grain boundaries (red arrows in Figure 4b,c).

Figure 4. SEM micrographs (3 kV) of the Ni/Si sample (**a**) before, (**b**,**c**) after ^{13}C implantation at 600 °C. The dark rectangle in (**b**) is zoomed in Figure 4c. The white and red arrows underline TLG fragments with one edge aligned with a grain boundary and crossing over a grain boundary, respectively.

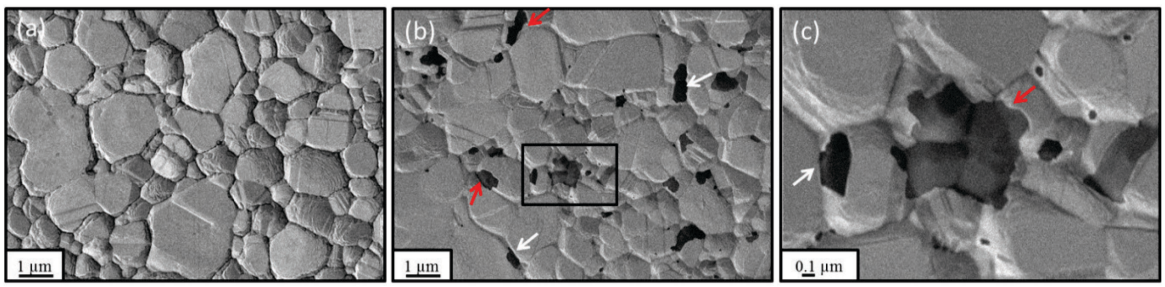

AFM images of the samples after the RTA treatment and the carbon implantation have also been obtained. As SEM images, they display a clear grain structure (Figure 5). The roughness has been determined as 35 ± 1 nm, 23 ± 2 and 27 ± 3 nm after carbon implantation at 450 °C (not shown), 525 °C (not shown), and 600 °C, respectively.

Figure 5. AFM images recorded on 10 × 10 µm^2. (Ni/Si) sample after RTA 900 °C and carbon implantation (20 keV, 4 EGM) at 600 °C.

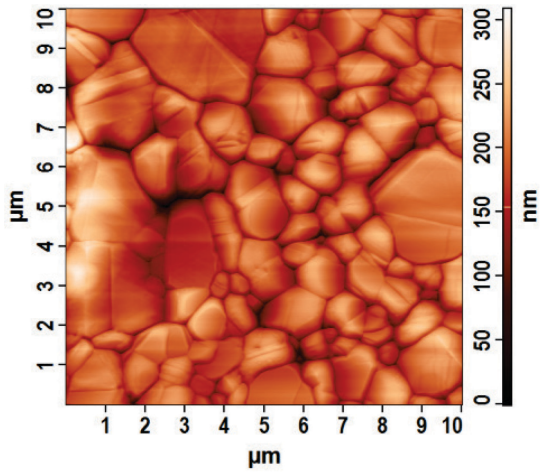

We have determined the size distribution of around 250 TLG pieces on the Ni/Si sample implanted at 600 °C (Figure 6). The maximum density peaks around 0.25 μm, but a long trail occurs, well above 1 μm, indicating that some coalescence of TLG likely happens.

Figure 6. TLG size distribution of the Ni/Si sample after ^{13}C implantation at 600 °C.

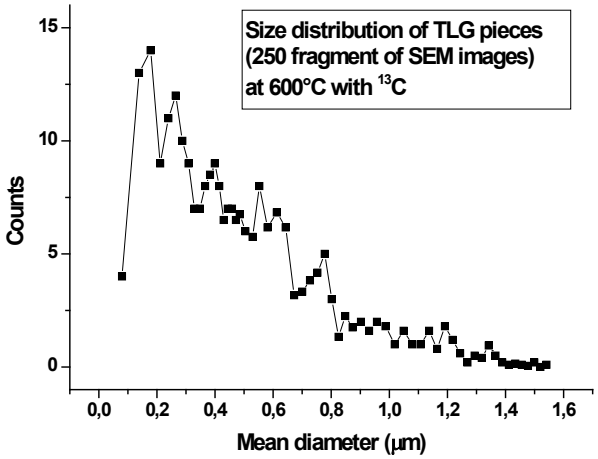

3.3. Raman Spectroscopy

A typical Raman spectrum is displayed in Figure 7, collected on the center of a TLG fragment.

Figure 7. Typical Raman spectrum obtained on a dark fragment on the Ni/Si sample annealed at 900 °C and implanted with 20 keV ^{12}C at 600 °C with 4 EGM.

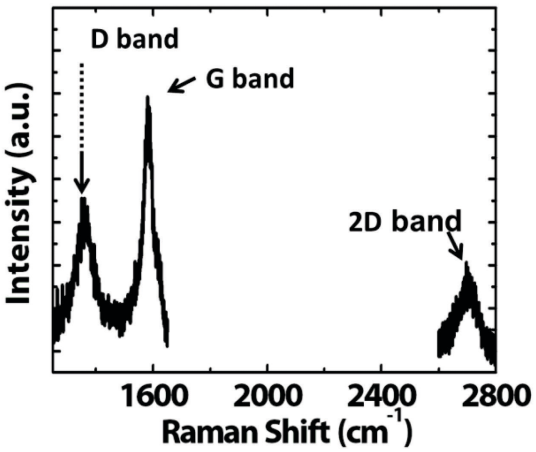

As expected, the Raman spectrum exhibits a D band at 1358 cm^{-1}, a G band at 1581 cm^{-1} and a 2D band around 2700 cm^{-1}. The G band is the one-mode Raman vibration characteristic of graphitic carbon [27]. The 2D band is a multiple step mode of carbon vibration in which intensity, shape, and wave number are sensitive to many parameters, such as the interaction with the substrate, the thickness of the graphene layers, the ordering within the graphene layers in the direction c normal to the graphene plan, and the presence of either impurities, doping atoms, vacancies, or functionalized molecules [23,28–31]. Finally, as soon as a graphitic domain displays either structural defects or size-limited dimensions, a D band will appear [32].

Figure 8b–d displays the corresponding mappings of the G, 2D, and D bands, respectively, obtained on the domain imaged in Figure 5a, speckled with dark TLG fragments. Pixel size is around 0.3×0.3 μm^2.

Figure 8. (**a**) Optical micrograph on the Ni/Si sample implanted at 600 °C ^{12}C at 20 keV; Raman mapping of the (**b**) G, (**c**) 2D, and (**d**) D bands. Note that the intensity scale of I_{2D} is half the ones of I_G and I_D.

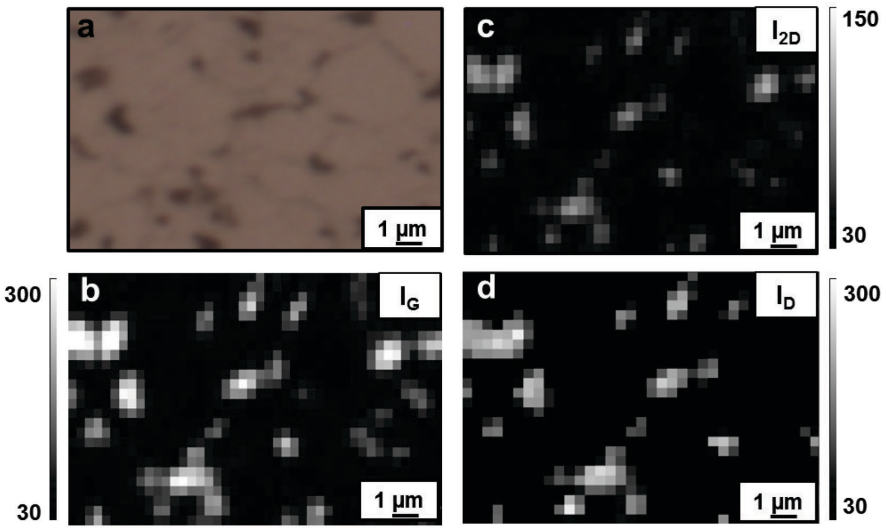

We can note the close correlation between the intensity of the G and D bands, whereas the 2D band is much less intense as the intensity scale of the former images are almost twice that of the latter. The appearance of this band is a clear indication that graphenization occurs at 600 °C, in contrast with lower temperatures (not shown). The weak intensity of the 2D is due to the poor ordering of the graphene plans in the c direction.

Moreover, in order to investigate the effect of isotopic labeling on the Raman spectra, a couple of samples were prepared with either ^{12}C or ^{13}C ions at an implantation energy of 20 keV, at 450 °C, 525 °C, and 600 °C, respectively. In Figure 9 we report in a panel the main features obtained on the sample implanted at 600 °C.

In Figure 9b typical Raman spectra are reported for the ^{12}C (blue) and ^{13}C (red) implanted samples on the dark fragments noted 1 in Figure 9a, respectively. In addition, a Raman spectrum of pure ^{13}C is reported (green), according to the wavenumber calculated with further Equation (2), in good agreement with those reported in [33] for a (^{12}C–^{13}C) bilayer graphene.

As expected, on the dark fragments, all the Raman bands (D, G, and 2D) exhibit a wavenumber downshift for the ^{13}C implanted sample. This downshift can be explained by phonon localization, due to elastic scattering of phonons by the ^{13}C atoms [34]. Single, but widened, contributions are observed for each band with the ^{13}C implanted Ni/Si samples, which can be explained by some mixing of ^{12}C and ^{13}C in the TLG [35].

In contrast, we never observed distinct contributions like those observed in a distinct (^{12}C–^{13}C) bilayer graphene [33]. For the ^{13}C implanted sample, the following contributions of the Raman red spectrum in Figure 9b are: a D peak at 1338 cm^{-1}, a G peak at 1555 cm^{-1}, and, finally, a 2D band at 2653 cm^{-1}, to be compared with the D, G, and 2D contributions of the ^{12}C implanted sample (blue

spectrum in Figure 9b) at 1358 cm^{-1}, 1581 cm^{-1}, and 2700 cm^{-1}, respectively. This downshift of the Raman wavenumber bands directly comes from the increase of the isotope mass as is reported in Equation (2), assuming random isotope repartition and equal bond force constants [36]:

$$\Delta\omega_i = (\omega_0 - \omega)_i = (\omega_0)_i \cdot \{1 - [(12 + c_0)/(12 + c)]^{1/2}\} \quad (2)$$

where ω_0 is the frequency of the given Raman mode i in the ^{12}C implanted sample, c and c_0 are the ^{13}C concentrations in the ^{13}C and ^{12}C samples (^{13}C natural abundance = 0.0107), respectively. The amplitude of this downshift has been experimentally confirmed on ^{12}C–^{13}C bilayer graphene [33]. The wavenumber shift (cm^{-1}), as a function of the ^{13}C concentration calculated according to Equation (2), is reported in Figure 10. It can be seen that the correlation is quasi linear. $(\omega_0)_i$ is quoted.as 1581 cm^{-1} in Figure 9b (blue line). Moreover, we noted that generally $\Delta\omega_{2D} \approx \Delta\omega_G$.

Figure 9. Raman spectroscopy on the ^{13}C implanted sample. (**a**) Optical micrograph; (**b**) experimental Raman spectra of ^{12}C (blue) and ^{13}C (red) implanted samples and theoretical Raman spectra of pure ^{13}C (green); (**c**,**d**) Raman mappings of the downward wavenumber shift of the 2D band (P_{2D}) and I_{2D}/I_G ratio, respectively. Pixel size is around 0.3 × 0.3 μm^2. The red dot in Figure 9a corresponds to the red spectrum in Figure 9b. The blue and red arrows in Figure 9c correspond to domains of low and high ^{13}C concentrations, respectively. The elliptic region in Figure 9a,c,d is a guide for the eye.

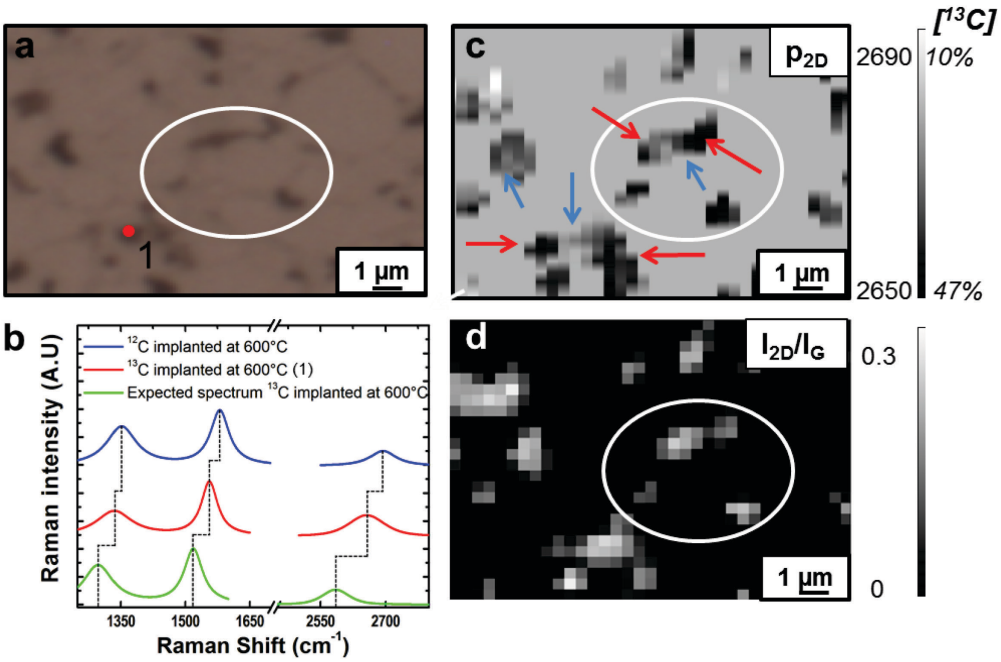

We have undergone Raman mappings over a 170 μm^2 area. The following procedures have been achieved with the ratio I_{2D}/I_G displayed in Figure 9d, as we must account for the absence of carbon over part of the surface. A minimal intensity of each Raman mode *i* (*i* = G, D, 2G) is evaluated $(A_{cutoff})_i$. All the pixels with an intensity lower than this cutoff intensity $(A_{cutoff})_i$ are set to zero. Any ratio $(I_{2D}/I_G)_i$ is equally set to zero when the denominator is lower than the cutoff intensity.

The 2D downshift (named as P_{2D} in Figure 9c) clearly points out to heterogeneities of the ^{13}C concentration inside a single TLG. The ^{13}C concentrations are in the range 20%–40%. Few of them display weaker ^{13}C concentrations.

Figure 10. Wavenumber shift (cm^{-1}) as a function of the ^{13}C concentration calculated according to Equation (2).

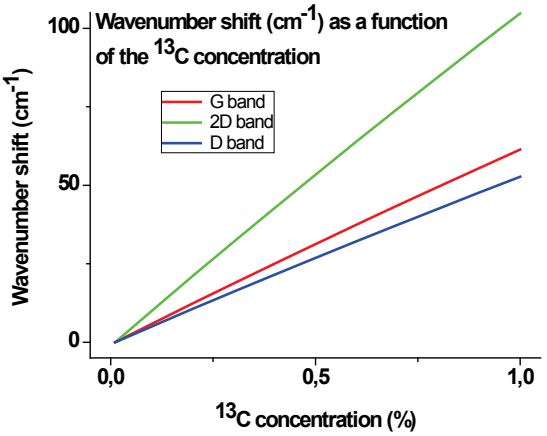

The I_{2D}/I_G ratio is expected to be sensitive to the thickness of the TLG [23]. The I_{2D}/I_G mapping given in Figure 9d also displays some heterogeneity inside a single one. Generally it is larger on the center. If the I_{2D} intensity line is correlated to the thickness of the TLG, this infers that the thickness of the TLG is also varying, even inside a single fragment.

The Full Width at Half Maximum (FWHM) of the G band typically ranges around 55–60 cm^{-1}, instead of 35–55 cm^{-1} for the ^{12}C implanted sample [20]. The large FWHM values are indicative of partial graphitic organization, which is expected for TLG not heated to more than 600 °C. Furthermore the broadening of the FWHM observed on the mixed (^{13}C–^{12}C) sample can be related to the mixing of ^{12}C and ^{13}C atoms inside a single fragment, in agreement with the absence of any splitting of the Raman mode.

The lowest ^{13}C concentrations are generally observed inside or at the sides of the fragment (blue arrows in Figure 9c), whereas the highest ^{13}C concentrations are observed at the sides of the fragment (red arrows in Figure 9c). In order to investigate more accurately the origins of these heterogeneities of the ^{13}C concentrations, we undertake Raman mappings on a larger TLG fragment (around 4 μm^2) involving around 60 pixels. Moreover the network of the grain boundaries has been determined around the TLG (Figure 11a). The boundaries have been tangentially extended below the TLG (Figure 11b).

This defined an area rich in grain boundaries on top and a large surface grain on the bottom of the TLG. The Raman mapping of the G band exhibits an increasing intensity from the side to the center of the TLG, with regular hexagonal shapes (Figure 11c). As the intensity of the G band is expected to be proportional to the graphene layers number, it is deduced that the TLG is then thicker in the center. By contrast the Raman mapping of the 13C concentration extracted from the wavenumber downshift of the G band does not exhibit uniform concentration (Figure 11d). The highest 13C concentrations are measured in the bottom of the fragment, matching the grain surface. The lowest 13C concentrations are found on top of the fragment where grain boundaries are expected. In addition, the Raman mapping of the ratio IG/ID follows more or less the same trend (Figure 11e). The ratio I2D/IG is restricted to the area above the grain surface and is rather uniform, in good agreement with the map of the G band (Figure 11f). Otherwise the intensity of the 2D band is too weak.

The implantation at lower temperatures (not shown) yields TLG with smaller sizes, highly defective (intense D band), and badly organized (absence or very weak 2D band) graphitic-like carbon.

Figure 11. Raman spectroscopy on the ^{13}C implanted sample. (**a**) Optical micrograph on a large scale displaying the network of grain boundaries; (**b**) Optical micrographon of a TLG with the grain boundaries (continuous lines) and the extrapolated grain boundaries below the TLG (dotted lines); (**c**) Raman mappings of (**c**) the G band; (**d**) the ^{13}C concentration obtained from the downward wavenumber shift of the G band; (**e**) the I_G/I_D and (**f**) I_{2D}/I_G ratio, respectively. Pixel size is around 0.3 × 0.3 μm^2.

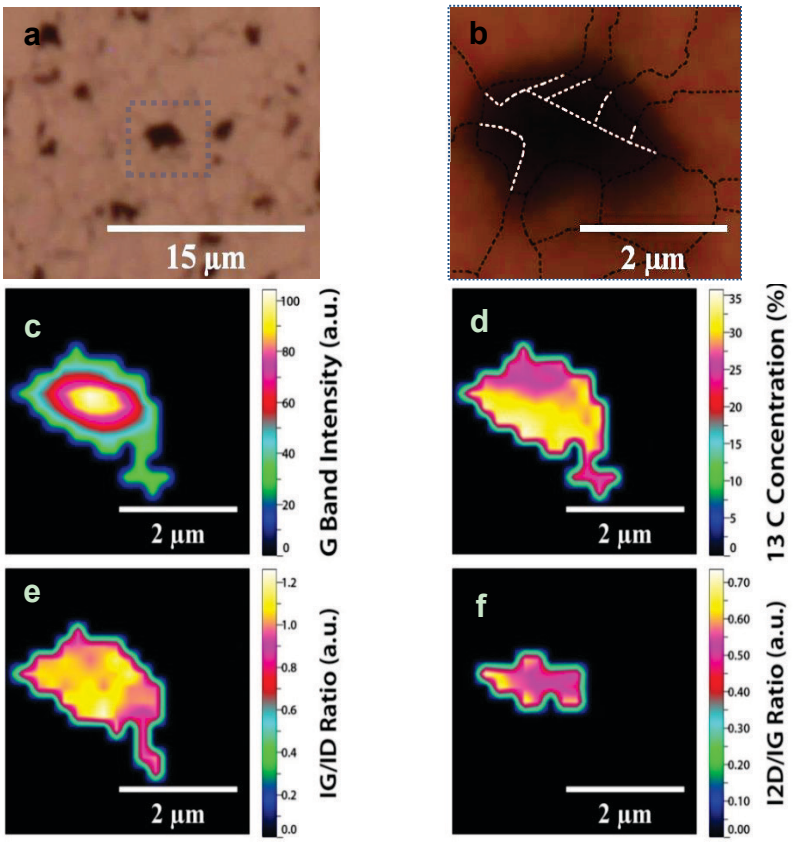

4. Discussion

The determination of the ^{13}C content by two independent probes, like NRA involving ^{12}C and ^{13}C isotopes, and Raman spectroscopy, help to elucidate the mechanism of formation of the TLG observed after carbon implantation at high temperature.

The best scenario to explain the results reported here assumes the previous presence of ^{12}C precursors, which act as nucleation centers. These ^{12}C atoms diffuse towards preferential nucleation centers as grain boundaries when the sample is heated. It must be noted that we cannot visualize TLG pieces after the RTA step. On the other hand, ^{13}C atoms, brought by implantation at high temperature, may aggregate to these nucleation centers during the heating and subsequent cooling. The mechanism of graphene formation has been described in the literature on nickel films by using isotopic labeling, starting from a $^{13}CH_4$ gas source [37]. It involves carbon bulk absorption and diffusion into the nickel film, followed by carbon surface segregation and precipitation of the carbon aggregates into graphene pieces (graphenization). At this stage it is important to distinguish between these two stages: (i) carbon surface segregation, without formation of graphitic-like fragment, and (ii) precipitation into graphene or TLG [38]. This mechanism does not include any nucleation process, but it is likely that ^{12}C still

existing at the surface may provide in our case the nucleation centers where the carbon surface first segregates. This can explained in that that, generally, a poor ^{13}C concentration is observed above the grain boundaries below the TLG. Further carbon, including ^{12}C incorporated into the nickel films as shown by NRA, and ^{13}C implanted further segregate to the surface and precipitate on these nucleation centers, forming a TLG that now expands towards the grain. Thus, area above the surface of the grain shows generally larger ^{13}C concentrations. It must be remembered, however, that a clear scrambling of the isotopic label occurs. In addition, it must be noted, however, that the pixel resolution in the Raman mapping is too poor to state if the carbon will aggregate to the nucleation center, either as atoms, giving complete random scrambling of the isotopes around the nucleation center, or as aromatic aggregates, giving distinct ^{12}C and ^{13}C 6-fold cycles. Clearly, further investigations are required to resolve this point. In conclusion the results reported here clearly support the mechanism of random carbon incorporation through carbon dissolution, carbon surface segregation, and surface precipitation of carbon aggregates into graphitic-like fragments, a mechanism postulated on nickel films. This is in contrast with the mechanism postulated on copper, where carbon precipitates directly as graphene on the surface. In this latter case, pure ^{12}C TLG pieces would be observed.

As shown by SEM, the nucleation centers are mainly located near microstructured defects like grain boundaries of nickel, preventing a uniform covering of the surface. This preferential nucleation is due to a rapid selective diffusion of carbon towards these defects. Therefore minimizing the grain boundaries, and other microstructural defects will get more uniform at the nucleation sites and consequently will improve the size of the domain.

Finally, it is interesting to compare the results of our Raman and NRA analyses for the mean determination of the ^{13}C concentration. First, one main interest of NRA is the measurement of the overall carbon concentration (bulk and surface) at each step of the process. Thus, we know that in addition to the ^{13}C implanted, some ^{12}C may have been incorporated before and during the carbon implantation. The Raman mapping yields ^{13}C concentrations are in the range 20%–40%, whereas the NRA result yields 40% (Table 1). This is rather a good agreement if we consider two main limitations. First, the NRA measurements of the ^{13}C isotope have a weak atomic cross section. Second, the reference G wavenumber in ^{12}C graphene-based films is sensitive not only to the atomic mass, but also to the thickness and the doping level [23].

5. Conclusions

In conclusion the main results of this study are:

The ^{12}C and ^{13}C nuclear reactions, used for the first time in the graphene field, allow the determining of the bulk and surface concentrations at any steps of the carbon implantation into a nickel film matrix. It also allows us to determine the origin of the carbon in the sample.

The combined use of NRA and Raman spectroscopy in the analysis of the thin layers graphene give some insight to the mechanistic process of TLG formation. Impurities of carbon aggregate through diffusion at high temperature on nucleation centers located in grain boundaries. Then, a mixture of ^{13}C and ^{12}C atoms or aggregates further precipitates into graphene fragments.

This preferential nucleation on grain boundaries leads to a non-uniform covering of the surface, in spite of a carbon in excess to the equivalent graphene monolayer. These results points to the need of

(i) a structure control of the Ni film minimizing microstructural defects; (ii) also a need to remove the carbon previously present at the surface and into the bulk of the nickel before carbon implantation. Works in this direction are presently in progress.

Acknowledgments

The authors gratefully acknowledge the helps of Chang Seok Lee for the sample preparation, Jacques Faerber for the SEM investigations and Yann Le Gall for carbon implantations.

Author Contributions

All the contributors have actively participated to the redaction of the paper. In addition Gaelle Gutierrez, Fitsum Aweke and Dominique Muller developed the NRA and RBS analyses, Fitsum Aweke the sample preparation, Raman imaging and AFM studies, Claude Speisser the SEM, Frédéric Antoni the Raman spectroscopy and François Le Normand the supervision of the entire work.

Conflicts of Interest

The authors declare no conflict of interest.

References

1. Avouris, P.; Dimitrakopoulos, C. Graphene: Synthesis and Applications. *Mater. Today* **2012**, *15*, 86–97.
2. Hernandez, Y.; Nicolosi, V.; Lotya, M.A.; Blighe, F.M.; Sun, Z.Y.; De, S.; MacGovern, I.T.; Holland, B.; Byrne, M.; Gunko, Y.K.; *et al*. High-Yield Production of Graphene by Liquid-Phase Exfoliation of Graphite. *Nat. Nanotechnol.* **2008**, *3*, 563–568.
3. Berger, C.; Song, Z.; Li, T.B.; Li, X.B.; Ogbazghi, A.Y.; Feng, R.; Dai, Z.; Marchenkov, A.N.; Conrad, E.H.; First, P.N.; *et al*. Ultrathin Epitaxial Graphite: 2D Electron Gas Properties and a Route Toward Graphene-Based Nanoelectronics. *J. Phys. Chem. B* **2004**, *108*, 19912–19916.
4. Emtsev, K.V.; Bostwick, A.; Horn, K.; Jobst, J.; Kellogg, J.L.; Ley, L.; Mac Chesnay, J.L.; Ohta, T.; Reshanov, S.A.; Rohrl, J.; *et al*. Towards Wafer-Size Graphene Layers by Atmospheric Pressure Graphitization of Silicon Carbide. *Nat. Mater.* **2009**, *8*, 203–207.
5. Obraztsov, A.N.; Obratzova, E.D.; Zolotukhin, A.A.; Tyurnina, A.V. Chemical Vapor Deposition of Thin Graphite Films of Nanometer Thickness. *Carbon* **2007**, *45*, 2017–2021.
6. Yu, Q.; Lian, Q.; Siriponglert, S.; Li, H.; Chen, Y.P.; Pei, S.S. Graphene Segregated on Ni Surfaces and Transferred to Insulators. *Appl. Phys. Lett.* **2008**, *93*, 113103–113106.
7. Reina, A.; Jia, X.; Ho, J.; Nezich, D.; Son, H.; Bulovic, V.; Dresselhaus, M.S.; Kong, J. Large Area, Few-Layer Graphene Films on Arbitrary Substrates by Chemical Vapor Deposition. *Nano Lett.* **2009**, *9*, 30–35.
8. Kim, K.S.; Zhao, Y.; Ahn, J.H.; Jang, H.; Lee, S.Y.; Kim, J.M.; Kim, P.; Choi, J.Y.; Hong, B.H. Large-Scale Pattern Growth of Graphene Films for Stretchable Transparent Electrodes. *Nature* **2009**, *457*, 706–710.

9. Chae, S.J.; Gunes, F.; Kim, K.K.; Kim, E.S.; Han, G.H.; Kim, S.M.; Shin, H.J.; Yoon, S.M.; Choi, J.Y.; Park, M.H.; *et al*. Synthesis of Large-Area Graphene Layers on Poly-Nickel Substrate by Chemical Vapor Deposition: Wrinkle Formation. *Adv. Mater.* **2009**, *21*, 2328–2333.
10. Baraton, L.; Maurice, J.L.; Lee, C.S.; Cojocaru, C.S.; Chatelet, M.; Pribat, D. On the Mechanisms of Precipitation of Graphene on Nickel Thin Films. *Europhys. Lett.* **2011**, *96*, 46003–46009.
11. Lee, C.S.; Cojocaru, C.S.; Moujahid, W.; Lebental, B.; Chaigneau, M.; Châtelet, M.; Le Normand, F.; Maurice, J.L. Synthesis of Conducting Transparent Few-Layer Graphene Directly on Glass at 450 °C. *Nanotechnology* **2012**, *23*, 265603–265609.
12. Mattevi, C.; Kim, H.K.; Chhowalla, M. A Review of Chemical Vapour Deposition of Graphene on Copper. *J. Mater. Chem.* **2011**, *21*, 3324–3334.
13. Sun, Z.; Zheng, Y.; Yao, J.; Beitler, E.; Zhu, Y.; Tour, J.M. Growth of Graphene from Solid Carbon Sources. *Nature* **2010**, *468*, 549–552.
14. Ruan, G.D.; Sun, Z.Z.; Peng, Z.W.; Tour, J.M. Growth of Graphene from Food, Insects, and Waste. *ACS Nano* **2011**, *5*, 7601–7607.
15. Garaj, S.; Hubbard, W.; Golovchenko, J.A. Graphene Synthesis by Ion Implantation. *Appl. Phys. Lett.* **2010**, *97*, 183103–183106.
16. Baraton, L.; Maurice, J.L.; Cojocaru, C.S.; Pribat, D.; He, Z.B.; Lee, Y.H.; Lee, C.S.; Gourgues-Lorenzon, A.F. Synthesis of Few-Layered Graphene by Ion Implantation of Carbon in Nickel Thin Films. *Nanotechnology* **2011**, *22*, 085601.
17. Mun, J.H.; Lim, S.K.; Cho, B.J. Local Growth of Graphene by Ion Implantation of Carbon in a Nickel Thin Film Followed by Rapid Thermal Annealing. *J. Electrochem. Soc.* **2012**, *159*, G89–G92.
18. Zhang, R.; Zhang, Z.D.; Wang, Z.S.; Wang, S.X.; Wang, W.; Fu, D.J.; Liu, J.R. Nonlinear Damage Effect in Graphene Synthesis by *C*-Cluster Ion Implantation. *App. Phys. Lett*. **2012**, *101*, 011905.
19. Zhang, Z.D.; Wang, Z.S.; Zhang, R.; Wu, X.Y.; Fu, D.J.; Liu, J.R. Improvement of Graphene Quality Synthesized by Cluster Ion Implantation. *Nucl. Inst. Meth. B* **2013**, doi:10.1016/j.nimb.2012.11.075.
20. Gutierrez, G.; Muller, D.; Antoni, F.; Speisser, C.; Aweke, F.; Le Gall, Y.; Lee, C.S.; Cojocaru, C.S.; Le Normand, F. Multi-Layer Graphene Obtained by High Temperature Carbon Implantation into Nickel Films. *Carbon* **2014**, *68*, 337–345.
21. Aweke, F.; Gutierrez, G.; Muller, D.; Lee, C.S.; Maurice, J.L.; Chaigneau, M.; Chatelet, M.; Cojocaru, C.S.; Le Normand, F. Graphene films by carbon implantation into nickel films and diffusion towards surface. submitted for publication, *J. Phys. Chem. C* 2014.
22. Stoquert, J.P.; Pêcheux, F.; Hervé, Y.; Marchal, H.; Stuck, R.; Siffert, P. VRBS: A Virtual RBS Simulation Tool for Ion Beam Analysis. *Nucl. Inst. Meth. B* **1998**, *136*, 1152–1158.
23. Ferrari, A.C.; Novoselov, K.S.; Geim, A.K.; Meyer, J.C.; Roth, S.; Scardaci, V.; Mauri, F.; Casiraghi, C.; Lazzeri, M.; Piscanec, S.; *et al*. Raman Spectrum of Graphene and Graphene Layers. *Phys. Rev. Lett.* **2006**, *97*, 187401–187406.
24. Huez, M.; Quaglia, L.; Weber, G. Fonction d'Excitation de la Réaction $^{12}C(d,p0)^{13}C$ entre 400 *et* 1350 keV—Distributions angulaires. *Nucl. Inst. Meth. B* **1972**, *105*, 197–203.
25. Colaux, J.L.; Thomé, T.; Terwagne, G. Cross Section Measurements of the Reactions Induced by Deuteron Particles on ^{13}C. *Nucl. Inst. Meth. B* **2007**, *254*, 25–29.

26. Hansen, M. *Constitution of Binary Alloys: Metallurgy and Metallurgical Engineering*, 2nd ed.; McGraw Hill Book: New York, NY, USA, 1958.
27. Tuinstra, F.; Koenig, J.L. Raman Spectrum of Graphite. *J. Chem. Phys.* **1970**, *53*, 1126–1131.
28. Malard, L.M.; Pimenta, M.A.; Dresselhaus, G.; Dresselhaus, M.S. Raman Spectroscopy in Graphene. *Phys. Rep.* **2009**, *473*, 51–87.
29. Pimenta, M.A.; Dresselhaus, G.; Dresselhaus, M.S.; Cancado, L.G.; Jorio, A.; Saito, R. Studying Disorder in Graphite-Based Systems by Raman Spectroscopy. *Phys. Chem. Chem. Phys.* **2007**, *9*, 1276–1291.
30. Cancado, L.G.; Jorio, A.; Ferreira, E.H.; Stavale, F.; Achete, C.A.; Capaz, R.B. Quantifying Defects in Graphene via Raman Spectroscopy at Different Excitation Energies. *Nano Lett.* **2011**, *11*, 3190–3196.
31. Calizo, I.; Bao, W.; Miao, F.; Lau, C.N.; Balandin, A.A. The Effect of Substrates on the Raman Spectrum of Graphene: Graphene-on-Sapphire and Graphene-on-Glass. *Appl. Phys. Lett.* **2007**, *91*, 1–4.
32. Ferrari, A.C.; Robertson, J. Resonant Raman Spectroscopy of Disordered, Amorphous, and Diamond like Carbon. *Phys. Rev. B* **2001**, *64*, 075414–075426.
33. Kalbac, M.; Fahrat, H.; Kong, J.; Janda, P.; Kavan, L.; Dresselhaus, M.S. Raman Spectroscopy and in Situ Raman Spectroelectrochemistry of Bilayer $^{12}C/^{13}C$ Graphene. *Nano Lett.* **2011**, *11*, 1957–1963.
34. Costa, S.D.; Fantini, C.; Righi, A.; Bachmatiuk, A.; Rummeli, M.H.; Saito, R.; Pimenta, M.A. Resonant Raman Spectroscopy on Enriched ^{13}C Carbon Nanotubes. *Carbon* **2011**, *49*, 4719–4723.
35. Rodriguez-Nieva, J.F.; Saito, R.; Costa, S.D.; Dresselhaus, M.S. Effect of ^{13}C Isotope Doping on the Optical Phonon Modes in Graphene: Localization and Raman Spectroscopy. *Phys. Rev. B*. **2012**, *85*, 1–8.
36. Fan, S.S.; Liu, L.; Liu, M. Monitoring the Growth of Carbon Nanotubes by Carbon Isotope Labeling. *Nanotechnology* **2003**, *14*, 1128–1135.
37. Li, X.; Cai, W.; Colombo, L.; Ruoff, R.S. Evolution of Graphene Growth on Ni and Cu by Carbon Isotope Labelling. *Nano Lett.* **2009**, *9*, 4268–4272.
38. Eizenberg, M.; Blakely, J.M. Carbon Monolayer Phase Condensation on Ni(111). *Surf. Sci.* **1979**, *82*, 228–236.